RSC Advances

RSC Publishing

PAPER

View Article Online
View Journal | View Issue

Pore-controlled synthesis of Mn_2O_3 microspheres for ultralong-life lithium storage electrode†

Cite this: *RSC Advances*, 2013, **3**, 1947

Liang Chang,[a] Liqiang Mai,*[ab] Xu Xu,[a] Qinyou An,[a] Yunlong Zhao,[a] Dandan Wang[a] and Xi Feng[a]

Received 1st November 2012,
Accepted 27th November 2012

DOI: 10.1039/c2ra22735e

www.rsc.org/advances

Mesoporous structures have attracted increasing interest in improving the cycling life and specific capacity of electrode materials. Mn_2O_3 microspheres with controlled pore size were successfully synthesized by morphology-conserved transformation at 500, 700 and 900 °C. Among them, mesoporous Mn_2O_3 microspheres annealed at 500 °C show the highest discharge capacity, the minor capacity fading per cycle and ultralong cycling life. It can realize 1000 stable charge/discharge processes with 125 mAh g^{-1} reversible capacity at current density of 1000 mA g^{-1}. Meanwhile, at relatively low current density (200 mA g^{-1}), it can deliver capacity of 524 mAh g^{-1} after 200 cycles. The remarkable electrochemical performance can result from the relatively high surface area and abundant surface active sites of mesoporous structure, which can enhance the continuous charge transfer kinetics, ion diffusion and capacity. The high cycling stability and long life span make mesoporous Mn_2O_3 microspheres promising electrode materials for electrochemical energy storage.

Introduction

With soaring power and energy needs for large-scale applications including portable electronic devices, next-generation plug-in hybrid electric vehicles, micro and nano electromechanical systems, lithium ion batteries (LIBs) have attracted much attention because of low self-discharge rate, high coulombic and energy efficiency, and no memory effect.[1–6] To meet the requirements of these applications, considerable efforts have been made to improve cycling life and capacity of electrode materials for LIBs.[7,8] Constructing appropriate structures, for instance, mesoporous structures,[9–11] hollow structures,[12–14] core/shell structures,[15–20] hierarchical heterostructures,[21,22] *etc.* is a feasible strategy to improve capacity and cycling performance of electrode materials. The key points are to reduce agglomeration during electrochemical cycling, decrease interfacial contact resistance and keep the pre-reserved voids to accommodate the volume change caused by Li ions intercalation/deintercalation. For these reasons, mesoporous nanomaterials can improve the surface areas, provide more active spots and increase lithium storage capacity, which are suitable electrode materials for long-life LIBs.

As anode materials for LIBs, 3d transition metal oxides have been considered as the promising candidates with higher capacity and longer cycling life than graphite.[23–25] The advantages can be attributed to the full electrochemical reduction of metal oxides that react with two or more Li per 3d metal, and internally nanostructured character of 3d metal oxides based on the formation of nanometer-metal cluster and Li_2O buffer matrix during conversion reaction. However, in the real situation, some obstacles limiting the cycling life still exist, such as the huge structural reorganization and volumetric changes, incomplete de-conversion due to the presence of inactive or electrically disconnected Li_2O/M regions and incomplete de-conversion to the initial valence of metal oxides. Therefore, it has seldom been reported that metal oxide electrodes of LIBs can realize 1000 times stable cycling.

Manganese oxides, as one of transition metal oxides, including MnO, MnO_2,[26,27] Mn_2O_3,[9,10] and Mn_3O_4,[28] have received great interest recently with the advantages of earth-abundant, non-toxic and cost effectiveness. Among them, Mn_2O_3 electrode materials for LIBs have a high theoretical capacity of 1018 mAh g^{-1} and lower operating voltage (average discharge voltage at 0.5 V and charge voltage at 1.2 V).[9] Herein, the main purpose of our experiment is to construct a proper structure to effectively improve the cycling life and stability of electrode materials by controlling synthesis conditions. $MnCO_3$ microspheres stacked with nanoparticles were synthesized as precursors by a hydrothermal method. Then a following thermal decomposition method was used to obtain

[a]*State Key Laboratory of Advanced Technology for Materials Synthesis and Processing, WUT-Harvard Joint Nano Key Laboratory, Wuhan University of Technology, Wuhan, 430070, P. R. China. E-mail: mlq518@whut.edu.cn; mlq@cmliris.harvard.edu*

[b]*Department of Chemistry and Chemical Biology, Harvard University, Cambridge, Massachusetts, 02138, USA*

† Electronic supplementary information (ESI) available: XRD patterns, TG-DTG curves and SEM images. See DOI: 10.1039/c2ra22735e

Mn_2O_3 microspheres with different pore structures at 500, 700 and 900 °C, respectively. As anode materials for LIBs, mesoporous Mn_2O_3 microspheres show excellent electrochemical performance in terms of high rate capability and long cycling behavior.

Results and discussions

The crystal structure of the as-synthesized precursor powders was characterized by X-ray diffraction (XRD) measurements. It can be seen from Fig. S1A, ESI,† all of the diffraction peaks can be indexed to the rhombohedral $MnCO_3$ (JCPDS Card No. 86-0173, space group: R_{3c}, $a = b = 4.772$ Å, $c = 15.6397$ Å, $\alpha = \beta = 90°$, $\gamma = 120°$). No impure phases have been detected. Because manganese has many valence states, a proper annealing temperature is significant to get the desired products. Thermogravimetric (TG) analysis was carried out in air before calcining the precursors to obtain Mn_2O_3 (Fig. S1B, ESI†). As shown in TG curves, there are three weight losses of 0.67% (I), 8.5% (II) and 22.9% (III) corresponding to the temperature range of ~200 °C, 200–400 °C and 400–550 °C, respectively. It may be attributed to the removal of water and ethanol molecules (I), the partial thermal decomposition of $MnCO_3$ to MnO (II) and the transformation process from $MnCO_3$ and MnO to Mn_2O_3(III). In particular, 500 °C is the critical temperature at which the decomposition of $MnCO_3$ and oxidation of MnO happened simultaneously.[29] Based on the TG results and analysis mentioned above, it is clear that Mn_2O_3 can keep thermal stability in the temperature range of 500–900 °C. Three different temperatures (500 (Sample 500), 700 (Sample 700) and 900 °C (Sample 900)) were chosen to calcine $MnCO_3$ precursors and the influences on crystallinity, pore size and electrochemical performance were also investigated. As shown in Fig. 1A, XRD patterns confirm that all products exhibit the same structure corresponding to cubic Mn_2O_3 (JCPDS Card No. 41-1442, space group: I_{a3}, $a = b = c = 9.4091$ Å, $\alpha = \beta = \gamma = 90°$). The sharp and strong XRD peaks demonstrate the good crystallinity and high purity of the products. In addition, according to the full width of half maximum (FWHM) based on the main diffraction peaks at (222), (440) and (211), the crystallinity of the samples increase along with the increasing annealing temperature.

Field emission scanning electron microscopy (FESEM) and transmission electron microscopy (TEM) images provide insights into the morphologies and detailed structures of the products. Sample 500 (Fig. 1B), Sample 700 (Fig. 1C) and Sample 900 (Fig. 1D) all keep the microsphere structure, consistent with the morphology of the precursors (Fig. S2, ESI†). It can demonstrate that the process is a morphology-conserved transformation. TEM image (Fig. 1E) has confirmed the microspheres of Sample 500 are piled up with nanoparticles, and pore structures exist both on the surface and in the internal part of microspheres. The results can be further confirmed by SEM images of a cross section of the microspheres shown in the insets of Fig. 1B and 1C. In addition, the lattice fringe spacings of 2.72 and 3.84 Å are recognized by high-resolution transmission electron microscopy (HRTEM) images (Fig. 1F and inset) and correspond to the inter plane distance of (222) and (211) of the cubic phase of Mn_2O_3, respectively. From wide view of SEM images of Fig. 1B, 1C and 1D, it could be seen that along with the increasing annealing temperature, the nanoparticles of the microspheres grew larger obviously and the diameter of the spheres decreased. This may be attributed to the aggregation and regrowth of the

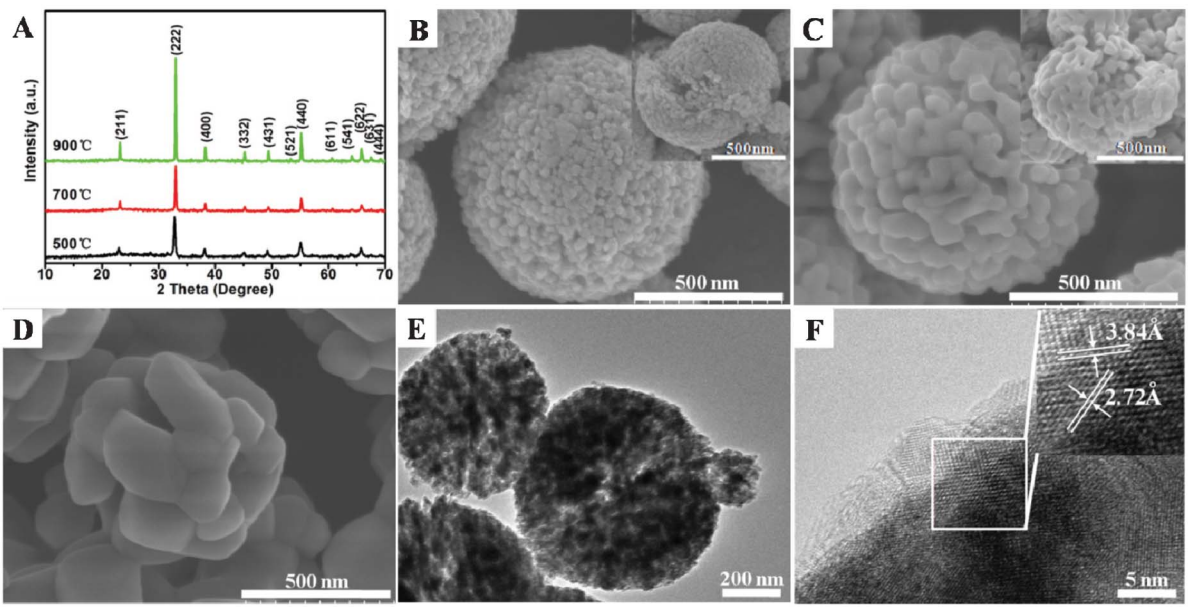

Fig. 1 (A) XRD patterns of Mn_2O_3 microspheres (B–D) SEM images of Mn_2O_3 microspheres annealed at 500, 700 and 900 °C, respectively. Insets in B and C are SEM images of corresponding cross section of microspheres. (E) TEM images and (F) HRTEM images Mn_2O_3 microspheres annealed at 500 °C.

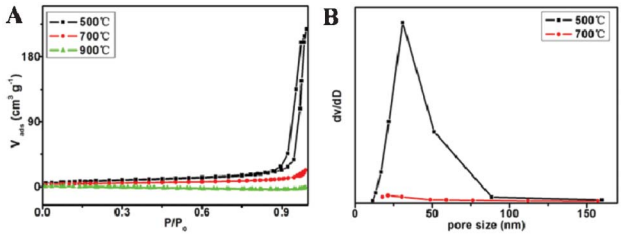

Fig. 2 (A) N_2 sorption isotherms of Mn_2O_3 microspheres and (B) their pore size distributions annealed at 500, 700 and 900 °C, respectively.

nanoparticles accompanying the pores that became larger and inhomogeneous (Sample 500 to Sample 700) until disappearing (Sample 900). To further determine the porous structure of the microspheres, we used nitrogen sorption isotherms for acquiring the pore parameters of Sample 500, Sample 700 and Sample 900. It is found that Sample 500 and Sample 700 have Brurauer–Emmerr–Teller (BET) surface areas of 28.3 and 16.1 $m^2\ g^{-1}$ with an average Barretl–Joyner–Halenda (BJH) pore diameter of 23.6 and 89.9 nm, respectively. The adsorption isotherms of Sample 500 and Sample 700 (Fig. 2A) appear to be type IV and type III curves respectively, with the same type III hysteresis loops. The results indicate the presence of a porous structure. For Sample 500, the pore size has a concentrated distribution at about 28 nm while for Sample 700, the pore size ranges from 0 to 170 nm (Fig. 2B). For the Sample 900, pore structure does not exist according to the very low BET surface areas and unavailable pore size data.

In order to determine the influence of pore structure and crystallinity on the electrochemical performance, the overall electrochemical performances are further tested. Cyclic voltammetry results for the Sample 500, 700 and 900 are shown in Fig. 3A. The voltammograms were measured at a sweep rate of 0.1 mV s^{-1} in the potential range from 3.0 to 0 V *vs.* Li/Li^+ at room temperature. It is obvious that the Sample 500 has larger curve area and higher redox peak current than those of Sample 700 and 900, suggesting the highest capacity and the fastest kinetics for Li ions insertion/extraction.[30–32] There is one couple redox peak, a reduction peak at 0.2 V and a wide oxidation peak at 1.2–2.2 V. The upper cutoff voltage is estimated to be 0.5 V, matching well with the galvanostatic charge/discharge profiles in Fig. 3B. For anode materials of LIBs, it is normal that electrolyte decomposed to form solid electrolyte interphase (SEI) layers on the surface of electrode materials corresponding to the peaks located at about 0.8 V in the first cathodic sweep. However, there is no peak existing at that potential. The phenomenon is consistent with Zhou's and Wang's report.[33,34] It may be attributed to the different surface properties of the electrode materials. Fig. 3B depicts the charge/discharge voltage profiles of Sample 500, 700 and 900 anodes for the first cycle at a current density of 200 mA g^{-1}. In the discharge curves, the first voltage drops from 3 to 0.5 V, which can be attributed to the reduction from Mn^{3+} to Mn^{2+} caused by Li ions insertion reaction. Then, the voltage slowly drops from 0.5 to 0 V that could be associated with the complete reduction from Mn^{2+} to Mn^0. For the charge curves, a wide slope existed between 1.2 V and 2.2 V which is related with oxidation of Mn^0 to Mn^{2+} and Mn^{2+} to Mn^{3+}, respectively. The relative equations are shown as follows (eqn 1–4).[9,10]

$$2Li^+ + 3Mn_2O_3 + 2e \rightarrow 2Mn_3O_4 + Li_2O \quad (1)$$

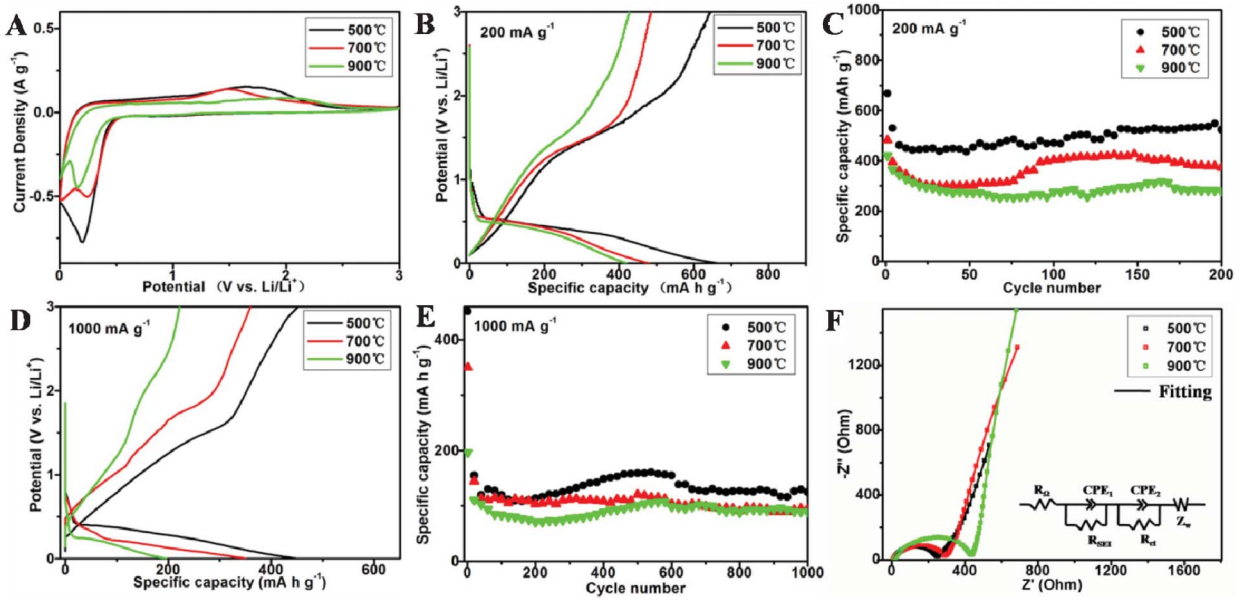

Fig. 3 (A) CV curves at a sweep rate of 0.1 mV s^{-1} in the potential range from 3.0 to 0 V *vs.* Li/Li^+. (B) The initial charge–discharge curves at the current density of 200 mA g^{-1}. (C) The cycling performance at the current density of 200 mA g^{-1}. (D) The initial charge–discharge curves at the current density of 1000 mA g^{-1}. (E) The cycling performance at the current density of 1000 mA g^{-1}. (F) AC-impedance spectra of Mn_2O_3 microspheres annealed at 500, 700 and 900 °C, respectively.

$$2Li^+ + Mn_3O_4 + 2e \rightarrow 3MnO + Li_2O \quad (2)$$

$$2Li^+ + MnO + 2e \rightarrow Mn + Li_2O \quad (3)$$

$$Mn + xLi_2O \rightarrow 2xLi^+ + MnO_x + 2xe(1.0 < x < 1.5) \quad (4)$$

The cycling performances of Sample 500, 700 and 900 at the current density of 200 mA g^{-1} are shown in Fig. 3C. The initial capacities of Sample 500, 700 and 900 are 668, 482 and 420 mAh g^{-1}, the discharge capacities at the 4th cycle of those are 529, 394 and 365 mAh g^{-1}, respectively. It is obvious that a large loss of capacities happened at the first few cycles which may be attributed to decomposition of electrolyte and irreversible phase transition. However, even after 200 cycles, the discharge capacities of Sample 500, 700 and 900 still remain 524, 373 and 279 mAh g^{-1}, corresponding to capacity retention of 99.1%, 94.6% and 76.4% and a capacity fading of 0.005%, 0.028% and 0.137% per cycle compared with capacities at the 4th cycle, respectively. Apparently, Sample 500 shows 200 cycles stable charge–discharge process with the best discharge capacity at the current density of 200 mA g^{-1} compared with not only Sample 700 and 900 but also those reported previously.[9,35–37]

High operation current density and long cycling life are necessary for the electrodes in hybrid electric vehicle applications. Here, by constructing a series of nanomaterials with controlled pore sizes, one goal is to effectively improve the cycling life of electrode materials with higher reversible capacity, another one is to investigate the pore structure and crystalline influence on electrochemical performance. It is clearly shown in Fig. 3D and E that Sample 500, 700 and 900 as anodes can realize 1000 cycles stable charge–discharge process at high current density (1000 mA g^{-1}). The 1000th discharge capacity can reach 125, 95 and 90 mAh g^{-1} for Sample 500, 700 and 900, respectively. Capacity retentions are 80.6%, 66% and 81.1% corresponding to the capacity fading of 0.022%, 0.042% and 0.021% per cycle compared with the 20th cycles, at which the discharge capacity of those are 155, 144 and 111 mAh g^{-1}, respectively. By analyzing the results of electrochemical performance, an interesting phenomenon can be seen that at the relatively low current density, the capacity retention order from high to low is Sample 500, 700 and 900 while the order is Sample 900, 500 and 700 at high current density. The probable explanations are as follows: (1) At relative low current density, Li ions insertion/extraction reactions happen not only on the surface but also in the inner part of the microspheres. Mesoporous structure provides a larger surface area, a shorter lithium ion insertion length and more active sites for lithium ions. Meanwhile, the existence of pore structure can accommodate the volume change properly and avoid the self-aggregation during charge–discharge.[38,39] For this reason, Sample 500 gets the best initial capacity, the maximum capacity retention and minimum capacity fading per cycle. (2) At a higher current density, Li ions insertion/extraction reactions mainly happen on the surface of electrode materials, so a larger surface area can provide more active sites for Li ions insertion/extraction and higher crystallinity can provide a more stable structure to accommodate the rapid insertion/extraction process of Li ions which are both beneficial for the high-rate charge–discharge process. It can be in good agreement with the results that Sample 500 with a mesoporous structure and Sample 900 with the highest crystallinity show the best capacity retentions and the least capacity fading per cycle at high current density. Therefore, the best electrochemical performance of Sample 500 is attributed to its high surface area and abundant surface defects that can enhance the continuous charge transfer kinetics, ion diffusion and capacity.[40,41] The results mentioned above can be supported by the electrochemical impedance spectroscopy (EIS) results (Fig. 3F). The charge transfer resistance of Sample 500 is 119 Ω, lower than the 165 Ω of Sample 700 and 433 Ω of Sample 900. As mentioned above, as anodes for the high-capacity and long life LIBs, electrode materials with mesoporous structures and a suitable degree of crystallinity are in favor of higher capacities and better stability at low or high current density.

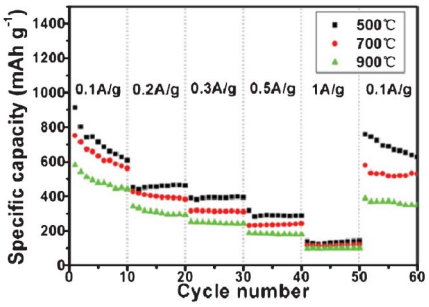

Fig. 4 Cycling specific capacity profile of Mn_2O_3 microspheres annealed at different temperatures.

To further investigate rate cyclability, the battery was charged and discharged at current density from 100, 200, 300, 500, 1000 mA g^{-1}, finally back to 100 mA g^{-1} (Fig. 4). All samples show good reversibility, indicating a degree of structural integrity during Li ions inseriton/deinsertion process, which can be further demonstrated by Fig. S4, ESI.† The microspheres of all samples can keep the integrated structure with few broken spheres. However, Sample 500 suffer the smallest volume change while Sample 900 suffer the largest one during the charge/discharge process. It can explain the advantages of a mesoporous structure as electrode materials on the other side. Meanwhile, Sample 500 with mesoporous structure shows high capacity. The corresponding discharge capacities varied accordingly with the discharge rates, changing from 913, 451, 391, 317 and 138 mAh g^{-1}, finally reversibly back to 760 mAh g^{-1}. Although the stability of Sample 500 is not the best when the current density was decreased from 1000 back to 100 mA g^{-1}, this phenomenon can be reasonably explained as follows. Compared to Sample 700 and 900, Sample 500 has more active materials to participate in the Li ions insertion/disinsertion process. Correspondingly, Li ions can insert into a deep position at low current density, and the deinsertion process become relatively hard. Therefore, Sample 500 need more cycles to

realize activation and stable charge/discharge process. In consideration of capacity, stability and cycling life, the excellent electrochemical performance of mesoporous Mn_2O_3 microspheres makes it a promising candidate as anode of LIBs.

Conclusions

In summary, Mn_2O_3 microspheres with controlled pore size have been successfully synthesized by morphology-conserved transformation at different annealing temperatures. Mesoporous structure, porous structure and non-porous structure have been obtained at 500, 700 and 900 °C, respectively. Among them, mesoporous structure can effectively improve the capacity of the electrode while high degree of crystallinity can provide the stable structure to enhance the stability of the electrode, especially at high current density. Therefore, by comprehensive consideration of the two factors, mesoporous Mn_2O_3 microsphere as the anode shows long cycling life, high capacity and relatively good stability because of its high surface area, abundant surface defects and high crystallinity. The reversible capacity can reach 125 mAh g^{-1} at a current density of 1000 mA g^{-1} and the cycling life can reach 1000 times. Therefore, the mesoporous Mn_2O_3 nanostructure is a promising candidate as anode material for long life, high-powered LIBs.

Experimental

Materials

$C_4H_6MnO_4{\cdot}4H_2O$, $C_{19}H_{42}NBr$ (CTAB), NH_4HCO_3, alcohol were analytical reagent grade, purchased from Sinopharm Chemical Reagent Co. Ltd., Shanghai, China. All chemicals were used as received without further purification.

Synthesis methods

In a typical synthesis, 2 mmol $C_4H_6MnO_4{\cdot}4H_2O$ and 0.028 g CTAB were added to the mixture of 24 mL ethanol and 24 mL distilled water. After the solution was gently stirred, 10 mmol NH_4HCO_3 was added to the homogeneously dispersed solution and stirred for 10 min. Then the reaction solution was transferred to a 100 mL Teflon-lined stainless steel autoclave and kept in an electric oven at 160 °C for 24 h. Later the autoclave was then taken out of the oven and left to cool naturally to room temperature. The obtained white-colored precursors were centrifuged, washed several times with distilled water and anhydrous ethanol, and dried at 60 °C in a vacuum oven. In order to get the Mn_2O_3 microspheres, all of the products were calcinated at 500, 700 and 900 °C for 3 h in air with a heating rate of 2 °C min^{-1}, respectively.

Characterization

XRD measurements were performed to investigate the crystallographic information using a D8 Advance X-ray diffractometer with non-monochromated Cu-Kα X-Ray source. FESEM images were collected with a Hitachi S-4800 at an acceleration voltage of 10 kV. TEM, HRTEM images were recorded by using a JEM-2100F STEM. Thermogravimetry/differential scanning calorimetry (TG/DSC) was performed using a Netzsch STA 449C simultaneous thermal analyzer at a heating rate of 10 °C min^{-1} in air. BET surface areas were measured using ASAP 3020 M instrument by adsorption of nitrogen at −209 °C.

Electrochemical measurement

The electrochemical properties were carried out by assembling 2025 coin cells in a glove box filled with pure argon gas, which used lithium pellets as the counter electrode and the reference electrode, a 1 M solution of $LiPF_6$ in ethylene carbon (EC)/dimethyl carbonate (DMC) (1 : 1 w/w) as electrolyte, cathode electrodes were obtained with 70% Mn_2O_3 microspheres active material, 20% acetylene black and 10% poly(tetrafluoroethylene) (PTFE). Galvanostatic charge/discharge cycling was studied in a potential range of 3.0–0 V *vs.* Li/Li^+ with a multichannel battery testing system (LAND CT2001A). CV and AC-impedance spectra were tested with an electrochemical workstation (CHI 760D).

Acknowledgements

This work was supported by the National Basic Research Program of China (2013CB934103, 2012CB933003), the National Natural Science Foundation of China (51272197 and 51072153), the International S&T Cooperation (2013ZR02930), the Program for New Century Excellent Talents in University (NCET-10-0661), and the Fundamental Research Funds for the Central Universities (2012-II-001, 2011-II-012). We are grateful to Prof. C. M. Lieber of Harvard University and Prof. Z. L. Wang of Georgia Institute of Technology for their strong support and stimulating discussions.

References

1 Z. G. Yang, J. L. Zhang, M. C. W. Kintner-Meyer, X. C. Lu, D. W. Choi, J. P. Lemmon and J. Liu, *Chem. Rev.*, 2011, **111**, 3577.
2 P. G. Bruce, B. Scrosati and J. M. Tarascon, *Angew. Chem., Int. Ed.*, 2008, **47**, 2930.
3 Y. Wang and G. Z. Cao, *Adv. Mater.*, 2008, **20**, 2251.
4 L. X. Yuan, Z. H. Wang, W. X. Zhang, X. L. Hu, J. T. Chen, Y. H. Huang and J. B. Goodenough, *Energy Environ. Sci.*, 2011, **4**, 269.
5 B. Z. Tian, X. L. Zheng, T. J. Kempa, Y. Fang, N. F. Yu, G. H. Yu, J. L. Huang and C. M. Lieber, *Nature*, 2007, **449**, 885.
6 S. Xu, Y. Qin, C. Xu, Y. G. Wei, R. S. Yang and Z. L. Wang, *Nat. Nanotechnol.*, 2010, **5**, 366.
7 L. Zhou, D. Y. Zhao and X. W. Lou, *Angew. Chem., Int. Ed.*, 2012, **51**, 239.
8 H. G. Jung, M. W. Jang, J. Hassoun, Y. K. Sun and B. Scrosati, *Nat. Commun.*, 2011, **2**, 516.
9 Y. C. Qiu, G. L. Xu, K. Y. Yan, H. Sun, J. W. Xiao, S. H. Yang, S. G. Sun, L. M. Jin and H. Deng, *J. Mater. Chem.*, 2011, **21**, 6346.

10 Y. F. Deng, Z. N. Li, Z. C. Shi, H. Xu, F. Peng and G. H. Chen, *RSC Adv.*, 2012, **2**, 4645.
11 X. M. Yin, L. B. Chen, C. C. Li, Q. Y. Hao, S. Liu, Q. H. Li, E. D. Zhang and T. H. Wang, *Electrochim. Acta*, 2011, **56**, 2358.
12 H. Wang, B. Li, J. Gao, M. Tang, H. B. Feng, J. H. Li and L. Guo, *CrystEngComm*, 2012, **14**, 3001.
13 J. S. Chen, L. A. Archer and X. W. Lou, *J. Mater. Chem.*, 2011, **21**, 9912.
14 F. Zhang, Y. Zhang, S. Y. Song and H. J. Zhang, *J. Power Sources*, 2011, **196**, 8618.
15 T. H. Hwang, Y. M. Lee, B. S. Kong, J. Seok Seo and J. W. Choi, *Nano Lett.*, 2012, **12**, 802.
16 L. W. Su, Z. Zhou and M. M. Ren, *Chem. Commun.*, 2010, **46**, 2590.
17 Y. Y. Cho, S. H. Lee, Y. S. Lee, T. Hong and J. Cho, *Adv. Energy Mater.*, 2011, **1**, 821.
18 H. Q. Li and H. S. Zhou, *Chem. Commun.*, 2012, **48**, 1201.
19 S. M Yuan, J. X. Li, L. T. Yang, L. W. Su, L. Liu and Z. Zhou, *ACS Appl. Mater. Interfaces*, 2011, **3**, 705.
20 Y. Li, S. M. Zhu, Q. L. Liu, J. J. Gu, Z. P. Guo, Z. X. Chen, C. L. Feng, D. Zhang and W. J. Moon, *J. Mater. Chem.*, 2012, **22**, 2766.
21 L. Q. Mai, F. Yang, Y. L. Zhao, X. Xu, L. Xu and Y. Z. Luo, *Nat. Commun.*, 2011, **2**, 381.
22 J. P. Liu, J. Jiang, C. W. Cheng, H. X. Li, J. X. Zhang and H. Cong, *Adv. Mater.*, 2011, **23**, 2076.
23 P. Poizot, S. Laruelle, S. Grugeon, L. Dupont and J. M. Tarascon, *Nature*, 2000, **407**, 496.
24 Y. Idota, T. Kubota, A. Matsufuji, Y. Maekawa and T. Miyasaka, *Science*, 1997, **276**, 1395.
25 P. L. Taberna, S. Mitra, P. Poizot, P. Simon and J. M. Tarascon, *Nat. Mater.*, 2006, **5**, 567.
26 C. J. Xu, C. G. Wei, B. H. Li, F. Y. Kang and Z. C. Guan, *J. Power Sources*, 2011, **196**, 7854.
27 J. F. Li, B. J. Xi, Y. C. Zhu, Q. W. Li, Y. Yan and Y. T. Qian, *J. Alloys Compd.*, 2011, **509**, 9542.
28 D. P. Dubal, D. S. Dhawale, R. R. Salunkhe, V. J. Fulari and C. D. Lokhande, *J. Alloys Compd.*, 2010, **497**, 166.
29 Y. F. Han, L. W. Chen, K. Ramesh, Z. Y. Zhong, F. X. Chen, J. H. Chin and H. W. Mook, *Catal. Today*, 2008, **131**, 35.
30 A. B. Yuan, S. A. Cheng, J. Q. Zhang and C. N. Cao, *J. Power Sources*, 1999, **77**, 178.
31 L. Q. Mai, X. Xu, C. H. Han, Y. Z. Luo, L. Xu, Y. M. Wu and Y. L. Zhao, *Nano Lett.*, 2011, **12**, 4992.
32 X. Xu, Y. Z. Luo, L. Q. Mai, Y. L. Zhao, Q. Y. An, L. Xu, F. Hu, L. Zhang and Q. J. Zhang, *NPG Asia Mater.*, 2012, **4**, e20.
33 L. Zhou, H. B. Wu, Z. Y. Wang and X. W. Lou, *ACS Appl. Mater. Interfaces*, 2011, **3**, 4853.
34 Z. Y. Wang, J. S. Chen, T. Zhu, S. Madhavi and X. W. Lou, *Chem. Commun.*, 2010, **46**, 6906.
35 M. Au and T. Adams, *J. Mater. Res.*, 2010, **25**, 1649.
36 Y. Cai, S. Liu, X. M. Yin, Q. Y. Hao, M. Zhang and T. H. Wang, *Phys. E.*, 2010, **43**, 70.
37 S. Nayak, S. Malik, S. Indris, J. Reedijk and A. K. Powell, *Chem.–Eur. J.*, 2010, **16**, 1158.
38 N. Li, G. Liu, C. Zhen, F. Li, L. L. Zhang and H. M. Cheng, *Adv. Funct. Mater.*, 2011, **21**, 1717.
39 Y. Li, S. M. Zhu, Q. L. Liu, J. J. Gu, Z. P. Guo, Z. X. Chen, C. L. Feng, D. Zhang and W. J. Moon, *J. Mater. Chem.*, 2012, **22**, 2766.
40 J. J. Auborn and Y. L. Barberio, *J. Electrochem. Soc.*, 1987, **134**, 638.
41 Y. M. Sun, X. L. Hu, W. Luo and Y. H. Huang, *J. Mater. Chem.*, 2012, **22**, 425.

